Acta Geotechnica
https://doi.org/10.1007/s11440-020-01138-w

RESEARCH PAPER

Design of a three-dimensional earth pressure device and its application in a tailings dam construction simulation experiment

Zhixiang Chen[1,2] · **Xiaoxia Guo**[1,2] · **Longtan Shao**[1,2] · **Shunqun Li**[3] · **Xiaojian Tian**[1,2]

Received: 21 February 2020 / Accepted: 30 December 2020
© The Author(s), under exclusive licence to Springer-Verlag GmbH, DE part of Springer Nature 2021

Abstract
The basic principle of the three-dimensional stress state test is deduced based on the relationship between the normal stress and the conventional stress state, and the relationship between the total stress state and the effective stress state is given based on Terzaghi's effective stress principle. On this basis, we made a three-dimensional earth pressure device by using a pedestal obtained by 3D printing technology, 6 micro earth pressure cells, a pore pressure cell and an attitude sensor. Considering the effect on the tested values of the dynamic change in the normal stress direction, the conversion relationship between the absolute test direction and the relative test direction of the test device is deduced, which can be used to dynamically test the three-dimensional total stress state and three-dimensional effective stress state. In addition, a method to calculate the K_0 value is proposed based on the earth pressure device comparing with the direct test result by the K_0 oedometer and indirect test results by direct shear test and triaxial test in laboratory. Two three-dimensional earth pressure devices are used in a simulation experiment of tailings dam construction, and the results show that with the increase in pore pressure, the calculated errors of the three-dimensional stress state caused by rotation angles will be more noticeable. This study has engineering value for in situ geotechnical testing and soil strength prediction.

Keywords Inverse matrix · K_0 value · Normal stress · Tailings dam · Three-dimensional earth pressure device

1 Introduction

The stress state is the basic index for evaluating the strength and deformation of soil and is also the vital monitoring index in geotechnical construction [6, 7, 11, 15]. The stress state of soil is a dynamic three-dimensional form, which is influenced by the scattered, multiphase, discontinuous and anisotropic soil properties [19, 31]. It is of great scientific significance and engineering value to reveal the evolution of the three-dimensional stress state of soil under external forces for the study of soil behavior.

Conventional stress test devices, such as earth pressure sensors and stress gauges, can only test the stress components in a certain direction. Clayton et al. [5] proposed diaphragm-type boundary total stress cells. Zhu et al. [31] proposed a new approach to conduct cell calibration and characteristic modeling and verified the applicability of miniature soil stress measuring cells in model tests. Horn & Johnson et al. [10] proposed a device to test the stress state in unsaturated soils without considering the angular rotation of the device. Several other test devices, such as the strain rosette pasting on the surface of a material [2, 4, 12], can also be used to test the three-dimensional stress state of continuous materials. However, soil is a typical discontinuous media. The nonlinear properties of deposition, creep, deformation, grain crushing, friction and the slip of particles in the loading process will make the behavior more complex [8, 20]; thus, the rotation of the test device in soil cannot be avoided. Hence, a stress state test device

✉ Xiaoxia Guo
hanyuer@dlut.edu.cn

[1] State Key Laboratory of Structural Analysis for Industrial Equipment, Dalian University of Technology, Dalian 116024, Liaoning, China

[2] Department of Engineering Mechanics, Dalian University of Technology, Dalian 116024, Liaoning, China

[3] Tianjin Key Laboratory of Soft Soil Characteristics and Engineering Environment, School of Civil Engineering, Tianjin Chengjian University, Tianjin 300384, China

Published online: 12 February 2021

in soil considering the effect of the device rotation during the test should be developed.

Numerous literature studies have proposed several devices to test the stress in different directions. The calibration procedures, sensor stiffness, electrical measurement method and application methods of the stress or pressure cells are usually undertaken [1, 5, 18, 21–26, 28, 31]. All the above studies can provide a foundation for the accurate measurement of earth pressures. On this basis, the test principle of the three-dimensional stress state is deduced based on the relationship between the normal stress and conventional stress state to explain that not all multidirectional pressure sensors can calculate the stress state. Moreover, the conversion relationship between the absolute test direction and the relative test direction of the test device is deduced to eliminate the test errors caused by the device rotation. On the basis of this theory, we made a three-dimensional earth pressure device (3D earth pressure device) consisting of a pedestal made by 3D printing technology, 6 pressure cells, a pore pressure cell and an attitude sensor. In addition, a method to calculate the K_0 value is proposed based on the 3D earth pressure device to connect the 3D earth pressure device with the strength parameters and to verify the test device. At last, this 3D earth pressure device was used in a simulation experiment of tailings dam construction.

2 Theory and method

2.1 Theory of the three−dimensional stress state

In three-dimensional space, the stress state of a point in the soil can be expressed by the stress component passing the point [13, 17]. Considering the symmetry of shear stress, the stress state of a point O can be expressed by 6 independent components, i.e., $\sigma_o = \{\sigma_x, \sigma_y, \sigma_z, \sigma_{xy}, \sigma_{yz}, \sigma_{zx}\}$. The normal stress σ in any direction through point O can be expressed by σ_o using the following equation [17].

$$\sigma = \sigma_x l^2 + \sigma_y m^2 + \sigma_z l^2 + 2\sigma_{xy} lm + 2\sigma_{yz} mn + 2\sigma_{zx} nl \qquad (1)$$

where σ is the normal stress, l, m, and n are the cosine values of the angles between the normal stress and the x-axis, y-axis, and z-axis, respectively.

If the normal stresses in 6 directions of a point are known, Eq. (1) can be expressed as a linear algebraic equation regarding σ_x, σ_y, σ_z, σ_{xy}, σ_{yz}, σ_{zx}, as shown in Eq. (2).

$$\left\{ \begin{array}{c} \sigma_a \\ \sigma_b \\ \sigma_c \\ \sigma_d \\ \sigma_e \\ \sigma_f \end{array} \right\} = \left\{ \begin{array}{cccccc} l_a^2 & m_a^2 & n_a^2 & 2l_a m_a & 2m_a n_a & 2n_a l_a \\ l_b^2 & m_b^2 & n_b^2 & 2l_b m_b & 2m_b n_b & 2n_b l_b \\ l_c^2 & m_c^2 & n_c^2 & 2l_c m_c & 2m_c n_c & 2n_c l_c \\ l_d^2 & m_d^2 & n_d^2 & 2l_d m_d & 2m_d n_d & 2n_d l_d \\ l_e^2 & m_e^2 & n_e^2 & 2l_e m_e & 2m_e n_e & 2n_e l_e \\ l_f^2 & m_f^2 & n_f^2 & 2l_f m_f & 2m_f n_f & 2n_f l_f \end{array} \right\} \left\{ \begin{array}{c} \sigma_x \\ \sigma_y \\ \sigma_z \\ \sigma_{xy} \\ \sigma_{yz} \\ \sigma_{zx} \end{array} \right\} \qquad (2)$$

which reduces to

$$\{\sigma_i\} = \boldsymbol{T}\{\sigma_j\} \qquad (3)$$

where $i = a, b, c, d, e, f$; $j = x, y, z, xy, yz, zx$; and $\boldsymbol{T}$ is a transition matrix, which is as follows:

$$\boldsymbol{T} = \left\{ \begin{array}{cccccc} l_a^2 & m_a^2 & n_a^2 & 2l_a m_a & 2m_a n_a & 2n_a l_a \\ l_b^2 & m_b^2 & n_b^2 & 2l_b m_b & 2m_b n_b & 2n_b l_b \\ l_c^2 & m_c^2 & n_c^2 & 2l_c m_c & 2m_c n_c & 2n_c l_c \\ l_d^2 & m_d^2 & n_d^2 & 2l_d m_d & 2m_d n_d & 2n_d l_d \\ l_e^2 & m_e^2 & n_e^2 & 2l_e m_e & 2m_e n_e & 2n_e l_e \\ l_f^2 & m_f^2 & n_f^2 & 2l_f m_f & 2m_f n_f & 2n_f l_f \end{array} \right\} \qquad (4)$$

If the existential conditions of inverse matrix $\boldsymbol{T}^{-1}$ are satisfied, the stress state of a point can be calculated from the normal stresses in 6 independent directions and the inverse matrix $\boldsymbol{T}^{-1}$, i.e.,

$$\{\sigma_j\} = \boldsymbol{T}^{-1}\{\sigma_i\} \qquad (5)$$

where $\boldsymbol{T}^{-1}$ is the inverse matrix of $\boldsymbol{T}$. If the inverse matrix $\boldsymbol{T}^{-1}$ of the transition matrix $\boldsymbol{T}$ exists, the test direction i ($i = a, b, c, d, e, f$) should be independent from each other. This means that the multidirectional pressure sensors should test at least 6 different directions before it can be used to calculate the stress state.

The effective stresses in any point of saturated soil can be computed from the total normal stresses and the pore water pressure, i.e., by Terzaghi's effective stress principle [27, 30]. Hence, the effective stress σ_i' in direction i can be expressed by the following equation:

$$\sigma_i' = \sigma_i - u \qquad (6)$$

where u is the pore water pressure in the soil. Introducing the 6 effective stresses σ_i' instead of the 6 normal stresses σ_i into Eq. (5), the three-dimensional effective stress state σ_j' can be calculated. To test the three-dimensional stress state of a soil, at least 6 independent normal stresses should be tested, while to compute the three-dimensional effective stress state, the pore water pressure of the test point should also be determined.

2.2 Dynamic test of the 3D earth pressure

In one-dimensional stress test, the test direction should be consistent with the design direction. Similarly, in the three-dimensional stress test, the space coordinate system (three axes) of the device should be consistent with the design one. The soil is a granular material with discontinuous, porous and multiphase properties [3, 8, 16]. The angles between the initial space coordinates and the current coordinates of the device can exist. To improve the testing accuracy, the initial coordinates should be dynamically consistent with the space coordinates of the test process (i.e., the angle between the current coordinate and the initial coordinate can be determined dynamically), especially in the embedment process after the position calibration.

The o_0-$x_0y_0z_0$ system is the absolute coordinate system that does not change with motion (Fig. 1). The o-xyz and o'-$x'y'z'$ systems are the initial coordinate system and the current coordinate system of the earth pressure device, respectively. In the embedment process, the o_0-$x_0y_0z_0$ system was set, and the o-xyz system is consistent with the o_0-$x_0y_0z_0$ system. During the test process, the o-xyz system rotates dynamically to the o'-$x'y'z'$ system under the effect of load or environment, while the o_0-$x_0y_0z_0$ system remains unchanged. The angle between the o-xyz and the o'-$x'y'z'$ systems will produce calculation errors in the three-dimensional stress state.

The rotation angle between the o-xyz and o'-$x'y'z'$ systems can be decomposed as the rotation angle around the z-axis, y-axis and x-axis, named θ, η and ζ. This rotation obeys the right-handed coordinate system (i.e., the rotation angle is positive if the rotation is in the counter-clockwise direction). The test direction of $\boldsymbol{i}$ ($i = a$, b, c, d, e, f) in Fig. 1 can be described as the vector $\vec{i}$ (x_i, y_i, z_i) from point $O(0, 0, 0)$ to point $P_i(x_i, y_i, z_i)$. The corresponding point $P_i'(x_i', y_i', z_i')$ of point $P_i(x_i, y_i, z_i)$ after rotation can be calculated by the rotation angles θ, η and ζ, as shown in the following Eq. (7):

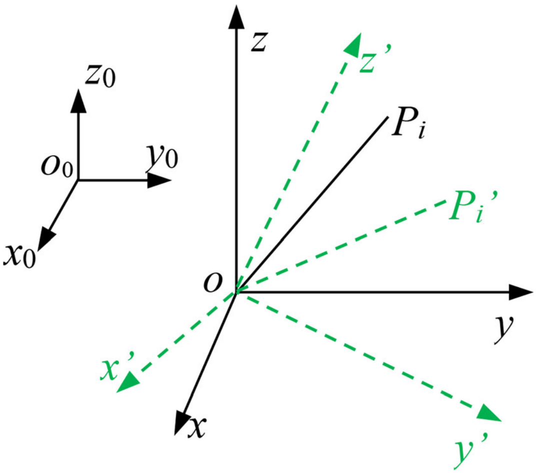

Fig. 1 The rectangular coordinate system and the device coordinates

$$\begin{bmatrix} x_i' \\ y_i' \\ z_i' \end{bmatrix} = \begin{bmatrix} \cos(\xi)\cos(\eta) & \sin(\xi)\cos(\eta) & -\sin(\eta) \\ \cos(\xi)\sin(\eta)\sin(\theta) - \sin\xi\cos\theta & \sin(\xi)\sin\eta\sin\theta + \cos(\xi)\cos(\theta) & \cos(\eta)\sin(\theta) \\ \cos(\xi)\sin(\eta)\cos(\theta) + \sin\xi\sin\theta & \sin(\xi)\sin\eta\cos\theta - \cos(\xi)\sin(\theta) & \cos(\eta)\cos(\theta) \end{bmatrix} \begin{bmatrix} x_i \\ y_i \\ z_i \end{bmatrix} \tag{7}$$

The new test direction of $\boldsymbol{i}'$ ($i' = a'$, b', c', d', e', f') at the o_0-$x_0y_0z_0$ system can be described by the point $O(0, 0, 0)$ and the point $P_i'(x_i', y_i', z_i')$, i.e., the vector $\vec{i}'(x_i', y_i', z_i')$. The cosine value $\{l_i', m_i', n_i'\}$ of $\vec{i}'$ can be calculated by the vector $\vec{i}'(x_i', y_i', z_i')$ and the unit vector at the x-axis $\vec{E}_x(1, 0, 0)$, y-axis $\vec{E}_y(0, 1, 0)$ and z-axis $\vec{E}_z(0, 0, 1)$, respectively, and the equations are as follows:

$$l_i' = \frac{\vec{i}' \cdot \vec{E}_x}{\left|\vec{i}'\right| \cdot |\vec{E}_x|} \tag{8}$$

$$m_i' = \frac{\vec{i}' \cdot \vec{E}_y}{\left|\vec{i}'\right| \cdot |\vec{E}_y|} \tag{9}$$

$$n_i' = \frac{\vec{i}' \cdot \vec{E}_z}{\left|\vec{i}'\right| \cdot |\vec{E}_z|} \tag{10}$$

Introducing the $\{l_i'' m_i'' n_i'\}$ of $\vec{i}'(i' = a', b', c', d', e', f')$ into Eq. (4), the matrix $\boldsymbol{T}'$ and the inverse matrix $\boldsymbol{T}^{-1'}$ can be calculated. Combining the tested values of σ_a' σ_b' σ_c' σ_d' σ_e' σ_f and the rotation angles ζ, η, θ, the dynamic three-dimensional stress state can be obtained by Eq. (5).

2.3 Design of the 3D earth pressure device

The 3D earth pressure device was made based on Eq. (5) and 3D printing technology. The structure of the pedestal was designed by the following procedures (Fig. 2): (1) A cube $M_1M_2M_3M_4$–$M_5M_6M_7M_8$ with l length on each edge was chosen, and the central points of six surfaces were named Q_1, Q_2, Q_3, Q_4, Q_5 and Q_6, respectively(Fig. 2a). (2) The midpoints of lines M_1M_5, M_2M_6, M_3M_7 and M_4M_8 were selected and named N_1, N_2, N_3 and N_4, respectively, and the midpoints of lines Q_1N_1, Q_1N_2, Q_1N_3, Q_1N_4, Q_2N_1, Q_2N_2, Q_2N_3 and Q_2N_4 were selected and named T_1, T_2, T_3, T_4, T_5, T_6, T_7 and T_8. (4) The diamond surfaces $Q_1T_1Q_2T_2$, $Q_1T_2Q_3T_3$, $Q_1T_3Q_4T_4$ and $Q_1T_4Q_1T_1$ were named a, b, c and d, respectively, and the diamond surfaces $T_2Q_2T_6Q_3$, $T_3Q_3T_7Q_4$, $T_4Q_4T_8Q_1$ and $T_1Q_1T_5Q_2$ were named e, f, g and

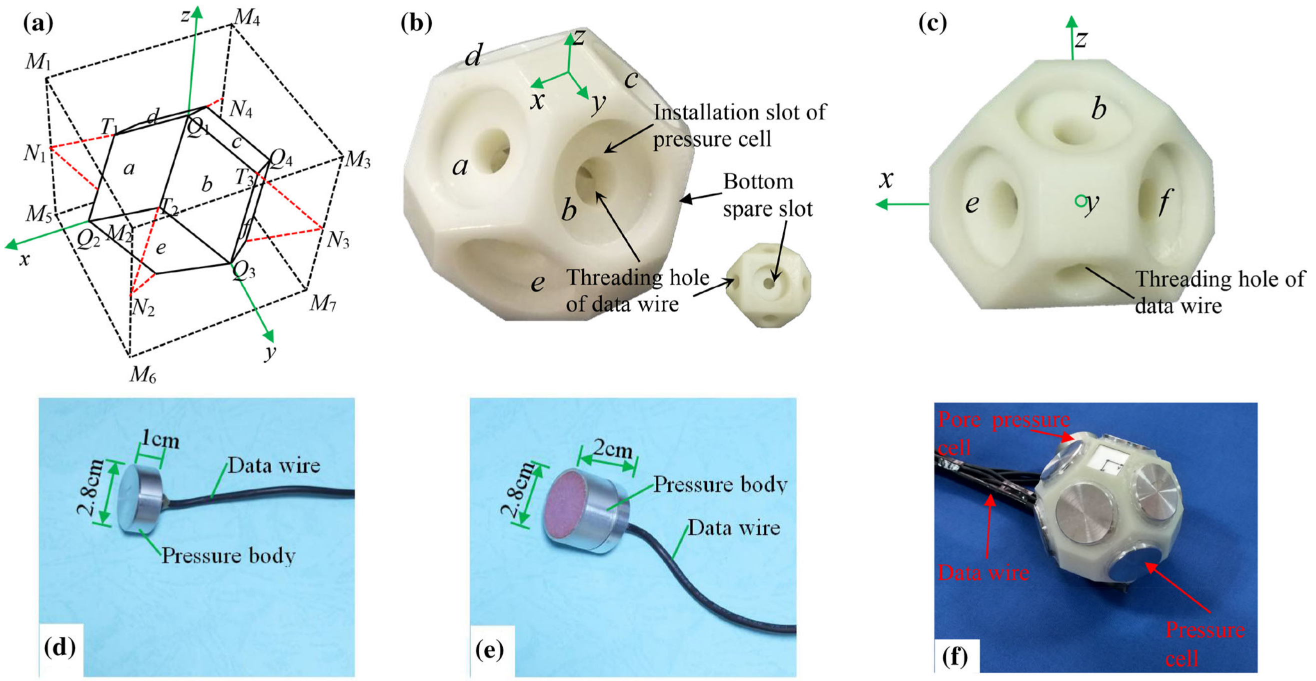

Fig. 2 Three-dimensional earth pressure device: **a** test structural; **b** pedestal photo; **c** side view of pedestal; **d** pressure cell; **e** pore pressure cell; **f** 3D earth pressure device

h. (5) The installation slots and threading holes were made on the surface (*a*, *b*, *c*, *d*, *e*, *f*, *g*, *h*), and the protruding cusps, including Q_1, Q_2, Q_3, Q_4, Q_5, Q_6, were cut to prevent stress concentration; the bottom parts which are symmetric about *a*, *b*, *c*, *d* were cut. A photograph of the pedestal is shown in Fig. 2b. Based on the rectangular coordinate system in Fig. 2b, the direction vectors of the 6 test directions can be deduced as in Table 1. Figure 2 and Table 1 show that the normal lines (test direction) of planes *a*, *b*, *c*, *d*, *e*, and *f* are independent of each other (satisfying the existing requirements of inverse matrix $\boldsymbol{T}^{-1}$ in Eq. (5)).

In one-dimensional earth pressure tests, in order to avoid overload and test errors of large range cells in low pressure stage, the measuring range of the test cell should be consistent with the stress range of the material to be tested. In the three-dimensional stress tests, in order to ensure test accuracy and the stability of the relative angles in the 6 test directions, both the measuring range of the test cell and the pedestal performance should be considered. If the stiffness of the pedestal is too small, the test unit will deform into the pedestal during the test, which will underestimate the earth pressure and change the relative angles in the 6 test directions. When the load is very small, the pedestal should be lighter than the soil to avoid the test error caused by its dead weight. In addition, the pedestal surface should be smooth to reduce the boundary friction. Hence, the pedestal should have the advantages of high stiffness, light weight and smooth surfaces.

The pedestal (weighing 137 g) in Fig. 2b was made using 3D printing technology, and the pedestal surface was covered with polytetrafluoroethylene (PTFE) to minimize boundary friction. The micro earth pressure cells and the pore pressure cell were selected and calibrated with the references [5, 30], and all the basic parameters of the pressure cells are shown in Table 2. In a compression test, the stiffness of the pedestal was found to be 1840 to 2000 times larger than that of the pressure cell diaphragm when the strain was 10 μm, which can ensure that the test values are not affected by the pedestal deformation in the test range of 0 to 0.18 MPa. The earth pressure cells and pore pressure cells were made by the Tianjin Shineway Science and Technology Co., Ltd. The micro attitude sensor was

Table 1 Direction vectors of three-dimensional earth pressure device

Direction vectors	*a*	*b*	*c*	*d*	*e*	*f*	*g*	*h*
l	$-1/\sqrt{2}$	0	$1/\sqrt{2}$	0	$-1/\sqrt{2}$	$1/\sqrt{2}$	$1/\sqrt{2}$	$-1/\sqrt{2}$
m	0	$-1/\sqrt{2}$	0	$1/\sqrt{2}$	$-1/\sqrt{2}$	$-1/\sqrt{2}$	$1/\sqrt{2}$	$1/\sqrt{2}$
n	$-1/\sqrt{2}$	$-1/\sqrt{2}$	$-1/\sqrt{2}$	$-1/\sqrt{2}$	0	0	0	0

Table 2 Basic parameters of pressure cell and attitude sensor

Cell/sensors	Test range	Test accuracy	Sizes	Signal type
Micro earth pressure cells	0–0.10 MPa	10^{-4} MPa	$d \times h = 28.00\ \text{mm} \times 10.00\ \text{mm}$	Strain gauge signal
Micro pore pressure cell	0–30.00 kPa	10^{-4} kPa	$d \times h = 28.00\ \text{mm} \times 10.00\ \text{mm}$	Strain gauge signal
Attitude sensor	− 180°–180°	0.01°	$L \times W \times H = 15.24\ \text{mm} \times 15.24\ \text{mm} \times 2.00\ \text{mm}$	RS-232

made by the Suzhou H-C Soil Water Science and Technology Co., Ltd.

The fabrication process of a 3D earth pressure device is as follows: (1) Place 6 micro earth pressure cells (Fig. 2d) in the installation slots of planes *a*, *b*, *c*, *d*, *e* and *f*. (2) Put a pore pressure cell (Fig. 2e) in the installation slot of plane *g* or plane *h*. (3) Fabricate a micro attitude sensor in the bottom spare slot of the pedestal. Thus, a 3D earth pressure device was formed (Fig. 2f). By using this 3D earth pressure device, normal stresses in 6 directions and the hydrostatic pressure of the test location were tested, and the rotation angles ζ, η and θ of the 3D earth pressure device can be tested by the micro attitude sensor. The three-dimensional stress state can be calculated based on Eq. (5).

Introducing the direction vectors (Table 1) of *a*, *b*, *c*, *d*, *e* and *f* into Eq. (4), the matrix $\boldsymbol{T}$ and inverse matrix $\boldsymbol{T}^{-1}$ can be obtained. The three-dimensional stress state before rotation (*o-xyz*) can be calculated as follows:

$$\begin{Bmatrix} \sigma_x \\ \sigma_y \\ \sigma_z \\ \sigma_{xy} \\ \sigma_{yz} \\ \sigma_{zx} \end{Bmatrix} = \begin{Bmatrix} 0.5 & -0.5 & 0.5 & -0.5 & 0.5 & 0.5 \\ -0.5 & 0.5 & -0.5 & 0.5 & 0.5 & 0.5 \\ 0.5 & 0.5 & 0.5 & 0.5 & -0.5 & -0.5 \\ 0 & 0 & 0 & 0 & 0.5 & -0.5 \\ 0 & 0.5 & 0 & -0.5 & 0 & 0 \\ 0.5 & 0 & -0.5 & 0 & 0 & 0 \end{Bmatrix} \cdot \begin{Bmatrix} \sigma_a \\ \sigma_b \\ \sigma_c \\ \sigma_d \\ \sigma_e \\ \sigma_f \end{Bmatrix} \tag{11}$$

where σ_a, σ_b, σ_c, σ_d, σ_e and σ_f are the test values of planes *a*, *b*, *c*, *d*, *e* and *f*. By using Eq. (6), the test values of the 6 earth pressure cells and the one pore pressure cell can be calculated. The effective normal stresses in 6 directions can also be calculated. Thus, the three-dimensional effective stress state before rotation (*o-xyz*) can be obtained by Eq. (11).

3 Application in a tailings dam construction simulation experiment

In order to verify the performance of this device, the 3D earth pressure device was used in a simulation experiment of tailings dam construction. Meanwhile, the mechanical parameters determined by this device were compared with the laboratory test values.

3.1 Details of the simulation experiment

A tailings dam is constructed by discharging tailings using the upstream method. From the dam body to the reservoir, considering that the early deposition properties of coarse particles can block the reverse impact of fine particles, the coarse particles were used as the bearing stratum of the future subdam (Fig. 3) to save construction investment and speed up solid deposition of the tailings. The tailings after mineral separation are a porous medium with a high moisture content, typically varying between 15–60%. The tailings were in the saturated state for a long time during the discharge and deposition processes.

In this test, the tailings reservoir will be used by two mining companies, while the particle compositions (Fig. 4) and flow rates (i.e., 39% and 18%, respectively, from different product parts) of the two mineral materials from the two mining companies are different. To ensure the safety of the reservoir and the dam, the two kinds of tailings should be mixed together and prepared for discharge on the dam. In the process of tailings discharge, the flow rate, deposition rate, and dissipation rate of the pore pressure can be reflected by the stress state and the effective stress state. By reducing the width of the dam on the site and considering the practice of the pipe discharge in turn (deposition height of each time less than 1 m), the test was simulated in a trough with a size of 300.00 m (length) × 1.50 m (width) × (1.50–2.00) m (height), as shown in Figs. 5 and 6. The internal side of the trough was a waterproof boundary (covered by waterproof geotextiles), while the bottom was a permeable boundary (dry beach formed by pre-deposited tailings). The waterproof geotextiles were buried at a certain depth off the bottom to

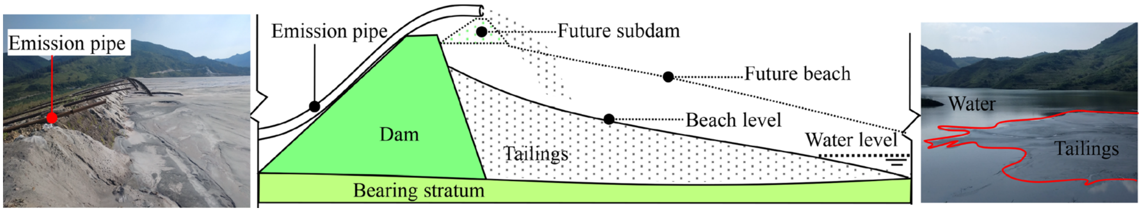

Fig. 3 Schematic diagram of tailings dam construction

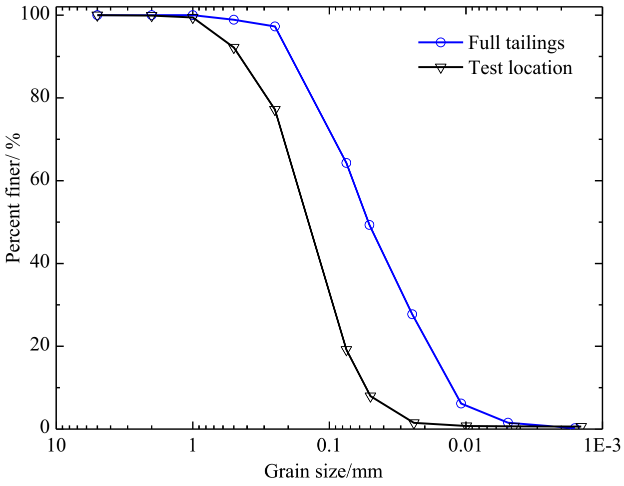

Fig. 4 Grain size distribution curve of tailings

prevent the water from flowing out from the junction part of the tank.

3.2 Application of the 3D earth pressure device

The buried location of the 3D earth pressure device is shown in Fig. 5, and the particle compositions of the tested location is shown in Fig. 4. The data wires of the 6 earth pressure cells, 1 pore pressure cell and 1 attitude sensor were connected to the acquisition system. The values of all the sensors were recorded by the computer connected with the acquisition system.

Firstly, the two kinds of tailings with different proportions were mixed in a cylindrical mixing facility with a diameter of 2 m (Fig. 6). Secondly, the mixed tailings were discharged to the trough until the test location reached a height of 10 cm. The bottom 3D earth pressure device was embedded in the midpoint of the dry beach (24 h interruption test). In the embedment process, a horizontal platform (lower than the midpoint of the dry beach) was cleaned on the dry beach with the aid of a leveling instrument, which made the coordinate system of the 3D earth pressure device parallel to the initial coordinate system on the horizontal platform (space coordinate system in Fig. 5), thus, the rotation angles θ, η and ζ of the device were calibrated as (0, 0, 0). Then, covering and consolidating the tailings on the 3D earth pressure device lightly, the rotation angles between the initial coordinates were recorded by the acquisition system in the covering process (rotation angles are shown in Fig. 7), and the angles of θ, η and ζ were set to zero (an optional operation) by consolidating the tailings, although imperfectly. After embedment, the tailings surface is consistent with the dry beach surface, to avoid the impact on the flow and consolidation of tailings. Then, the mixed tailings were discharged to the trough until reaching the buried height at the top of the 3D earth pressure device. The top of the 3D earth pressure

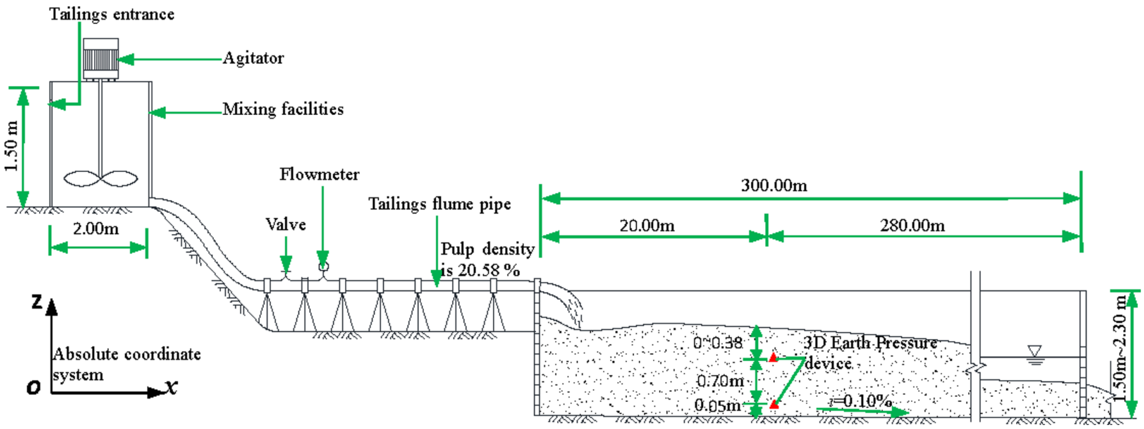

Fig. 5 Embedded position of three-dimensional earth pressure devices

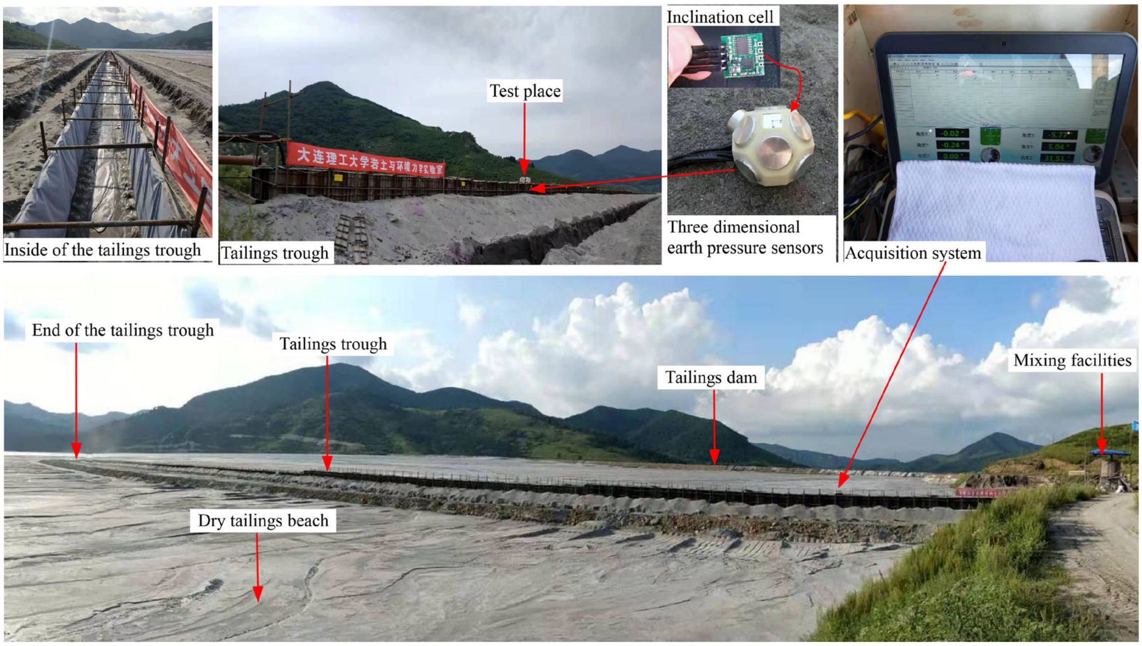

Fig. 6 Photograph of simulation experiment of tailings dam construction

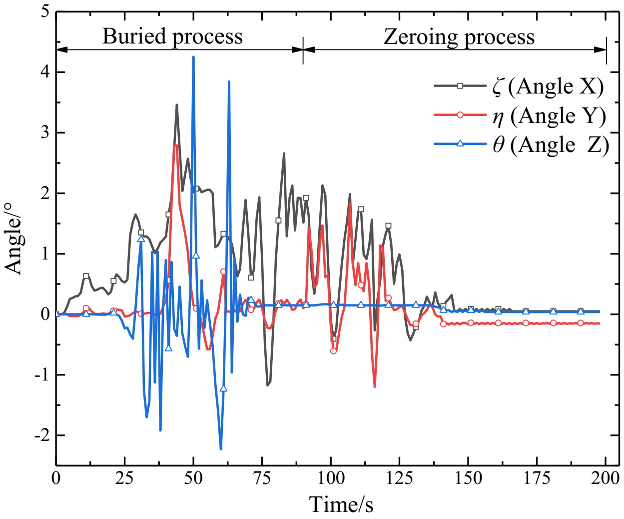

Fig. 7 Rotation angles of the test device in the embedded process

device was embedded in the midpoint of the tailings (After 30-min interruption test, the deposited surface can bear the load of a 75 kg man), and its burial method is the same as that of the device at the bottom.

The bottom 3D earth pressure device worked from Aug. 21, 2019 to Sept. 10, 2019 (from 0d to the end), and the top 3D earth pressure device worked from 10.9d to the end. The discharge process of the mixed tailings was stopped 10 times affected by the production process. From 20d to the end, we applied a 200 kg load with an area of 0.5 m (length) × 0.5 m (width) on the tailings above the upper 3D earth pressure device to observe the behavior of the external load on the consolidation of the tailings. The 10 time intervals and the test details are listed in Fig. 8. The pressure values in 6 directions, the pore pressure values, and the rotation angles of θ, η and ζ are shown in Fig. 9.

4 Results and analysis

Figure 7 shows that the rotation angle that affects the test results cannot be avoided in the embedded process. The value of θ reached 4°, and the values of η and ζ also reached 3°. Therefore, the consideration on the correction of the dynamic change in angles was suitable and necessary. Figure 9 shows that the angles will rotate with time during the testing and loading processes, in addition, the changes in angles will be aggravated with the monitoring process. The changes of η and ζ were significantly greater than those of θ in both the bottom and the top devices, which indicates that the soil is more inclined to produce the angle difference caused by uneven settlement than to rotate in a certain horizontal plane. The test values of a, b, c, and d are different while they are nearly at the same height and symmetrical angles, which shows that the anisotropy of the load distribution still exists in the flow and deposition process of tailings. The test values show that the earth pressure cell in directions a, b, c, and d approximately obeys $a \geq d \geq c \geq b$, and all the earth pressure test values are larger than that of the pore water pressure.

The angle X (ζ) is rotated gradually to negative, and the test value in direction d is much larger than that in direction b. Compared with the rigid boundary in directions b and d,

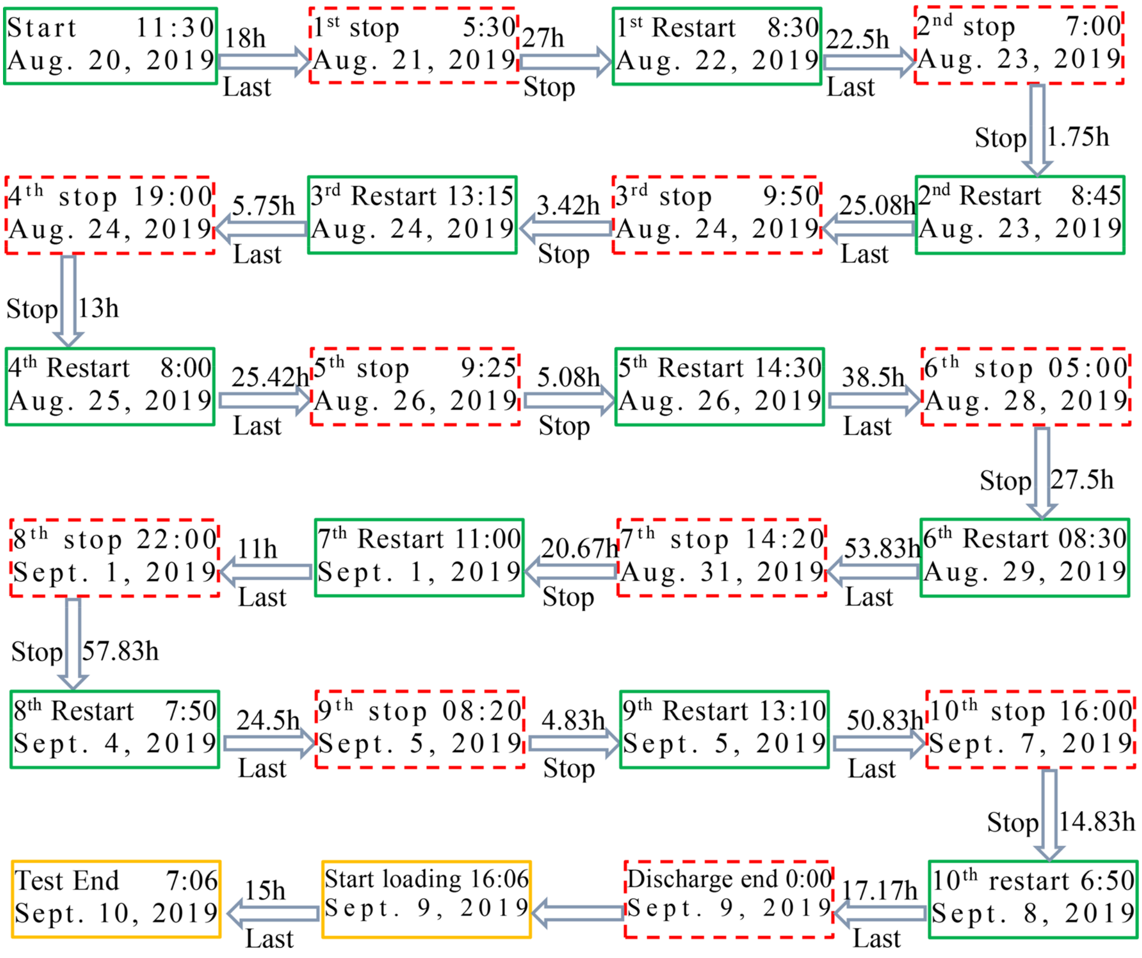

Fig. 8 Tailings emission process and testing process

directions *a* and *c* are more susceptible to the transverse effect of tailings flow. Hence, the pressures in directions *a* and *c* are larger than those in directions *b* and *d*. Because the angle *Y* (***θ***) is rotating gradually to negative (i.e., the direction *a* is more parallel to the Z-axis), the pressure in direction *a* is larger than that in direction *c*. In summary, the rotation angles affect not only the prediction accuracy of the initial coordinate system but also the scientificity of the test values. Compared with the test values of the bottom 3D earth pressure device (Fig. 9c), the test values of the top 3D earth pressure device (Fig. 9d) increased rapidly during the loading stage (20 d to the end), which is consistent with the diffusion law of additional stress.

The three-dimensional stress state and the three-dimensional effective stress state can be calculated with Eq. (11). Similarly, using Eq. (5) to Eq. (10), the three-dimensional stress state and the three-dimensional effective stress state, which consider the effects of the rotation angles of the 3D earth pressure device, can be calculated, and the results and the numerical differences between different calculation methods are shown in Figs. 10 and 11.

Figures 10 and 11 show that the values of normal stress and shear stress at different depths increase gradually with the continuation of the test process. The differences between the 3 normal stresses are small at the small depth of the tailings deposited on the upper 3D earth pressure device (see Fig. 5). Along with the increase of the upper deposition load, the vertical force (σ_z) is larger than the force (σ_x) in the flow direction, and the force (σ_x) in the flow direction is larger than that (σ_y) at the lateral boundary, while σ_x and σ_y are at the same horizontal height. The same conclusions can be obtained considering the influence of pore water pressure on the test results (Figs. 10b and 11b).

Comparing the three-dimensional stress state [$\boldsymbol{\sigma}_{11}$] with the three-dimensional effective stress state [$\boldsymbol{\sigma}_{12}$] (Figs. 10c and 11c), it can be found that the stress [$\boldsymbol{\sigma}_{12}$] constitutes the vast majority of the total stress [$\boldsymbol{\sigma}_{11}$], and the pore pressure affects the normal stress but does not affect the magnitude of the shear stress (Figs. 10c, d, 11c, d). The stress errors of three normal stresses affected by pore water pressure are consistent, and the values are consistent with the pore

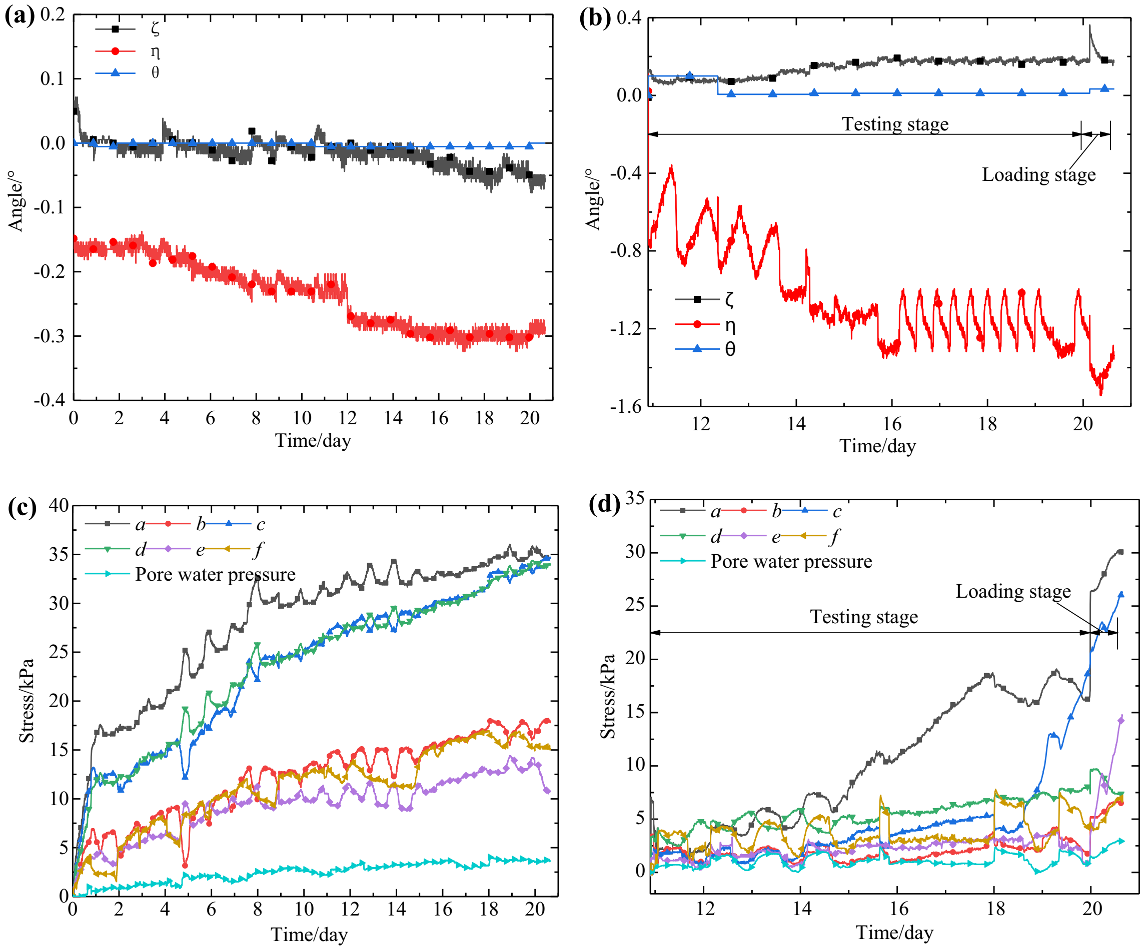

Fig. 9 Test values of the 3D earth pressure devices: **a** rotation angles of the bottom device; **b** rotation angles of the top device; **c** value of pressure cells on the bottom device; **d** value of pressure cells on the top device

water pressure. The errors of three-dimensional stress state are affected by the rotation angles (Figs. 10g, h, 11g, h), and this influence will increase with the increase of test values and rotation angles. Figures 10i and 11i show that, there is a correlation between the stress errors and the test values, i.e., the larger the value of normal stress is, the greater the error is, in addition, the greater the absolute value of shear stress is, the greater the error is.

Figures 10 and 11 show that, the average errors and standard deviations of the stress errors caused by pore water pressure are consistent, regardless of the rotation angles; and the average errors and standard deviations of stress errors caused by rotation angles are also consistent, regardless of the pore water pressure. When considering the both effects of pore water pressure and rotation angles, the errors of normal stresses are close to those caused by pore water pressure, and the errors of shear stresses are consistent with those caused by rotation angles. Therefore, it can be proven that, the pore water pressure does not affect the shear stress, while the rotation angle has a greater influence on the normal stress.

The three-dimensional stress state can be expressed in different space coordinate systems, and those values will be dependent on the coordinate systems. Literature studies show that, the stress state of a point can be expressed by three principal stresses, and those directions can be expressed by the direction cosines. On the basis of $[\boldsymbol{\sigma}_{22}]$ in Fig. 10 and Fig. 11, and the equation $l_k^2 + m_k^2 + n_k^2 = 1$, the principal stresses (σ_1, σ_2, σ_3) and the stress directions (l_k, m_k, n_k) ($k = 1, 2, 3$) can be calculated by the three-dimensional stress state, and the results are shown in Fig. 12. The σ_1, σ_2 and σ_3 in Fig. 12 increase gradually with the increase of time and load, and has the similar evolution trend with the three normal stresses (σ_x, σ_y, σ_z). The direction cosine expresses the relationship between the principal stress and the initial coordinate system. When the additional load on the tailings is small or instantaneous, the direction cosine transformation is complex, and even occurs a shift in the stress direction. With the increase of

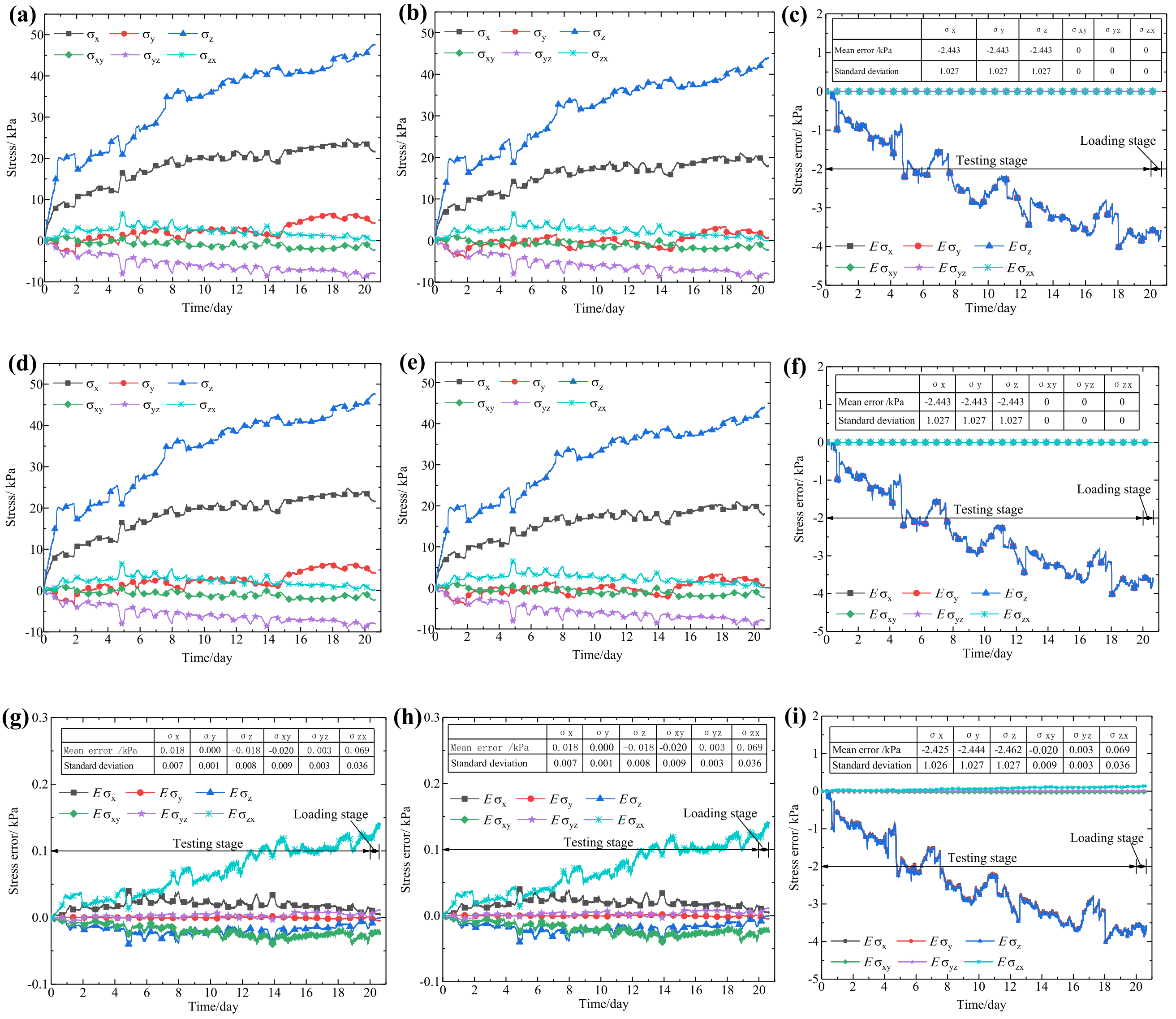

(c)

	σ x	σ y	σ z	σ xy	σ yz	σ zx
Mean error /kPa	-2.443	-2.443	-2.443	0	0	0
Standard deviation	1.027	1.027	1.027	0	0	0

(f)

	σ x	σ y	σ z	σ xy	σ yz	σ zx
Mean error /kPa	-2.443	-2.443	-2.443	0	0	0
Standard deviation	1.027	1.027	1.027	0	0	0

(g)

	σ x	σ y	σ z	σ xy	σ yz	σ zx
Mean error /kPa	0. 018	0.000	−0. 018	-0.020	0. 003	0. 069
Standard deviation	0.007	0.001	0.008	0.009	0.003	0.036

(h)

	σ x	σ y	σ z	σ xy	σ yz	σ zx
Mean error /kPa	0. 018	0.000	−0. 018	-0.020	0. 003	0. 069
Standard deviation	0.007	0.001	0.008	0.009	0.003	0.036

(i)

	σ x	σ y	σ z	σ xy	σ yz	σ zx
Mean error /kPa	-2.425	-2.444	-2.462	-0.020	0.003	0.069
Standard deviation	1.026	1.027	1.027	0.009	0.003	0.036

Fig. 10 Calculated results of the three-dimensional stress state of the bottom device: **a** total stress state [σ_{11}]; **b** effective stress state [σ_{12}]; **c** [σ_{12}]–[σ_{11}]; **d** total stress state considering rotation angles [σ_{21}]; **e** effective stress state considering rotation angles [σ_{22}]; **f** [σ_{22}]–[σ_{21}]; **g** [σ_{21}]–[σ_{11}]; **h** [σ_{22}]–[σ_{12}]; **i** [σ_{22}]–[σ_{11}]

additional load, the principal stress direction is gradually stable.

Literature studies enhanced the theory to calculate the stress state in soils, while it is difficult to simulate the stress state in the gradual increase process considering the anisotropy behaviors. To verify the reliability of the three-dimensional stress state test results, an indirect method was used to compare the test results with the strength parameters tested in the laboratory. The verification procedure is as follows: (1) calculate the K_0 value by the results of the three-dimensional stress state; (2) use the K_0 value to calculate the friction angle (φ) of the tailings material; and (3) test and compare the values of K_0 and friction angle (φ) of the tailings by different laboratory test methods.

By using the relationship among σ_z, σ_x and σ_y, the K_0 value was obtained from Fig. 10e. As shown in Fig. 13, the blue line indicates the relationship between σ_x and σ_y, and the green line indicates the relationship between σ_y and σ_z. Meanwhile, the K_0 value of the in situ tailings can be tested in laboratory with the K_0 oedometer (GBSL237-1999) [9, 14], and the result is shown by the dotted red line in Fig. 13. Because the tailings in the test location are a sand (Fig. 4), and using the Jaky's formula [$K_0 = 1 - \sin(\varphi)$] for sand, the value of K_0 can be estimated based on the friction angle (φ). Based on the direct shear test and triaxial test, the tailings taken from the testing site were tested with a dry density of 1.725 g/cm^3 (the in situ density), and the comparison of φ and K_0 are shown in Table 3. Setting the

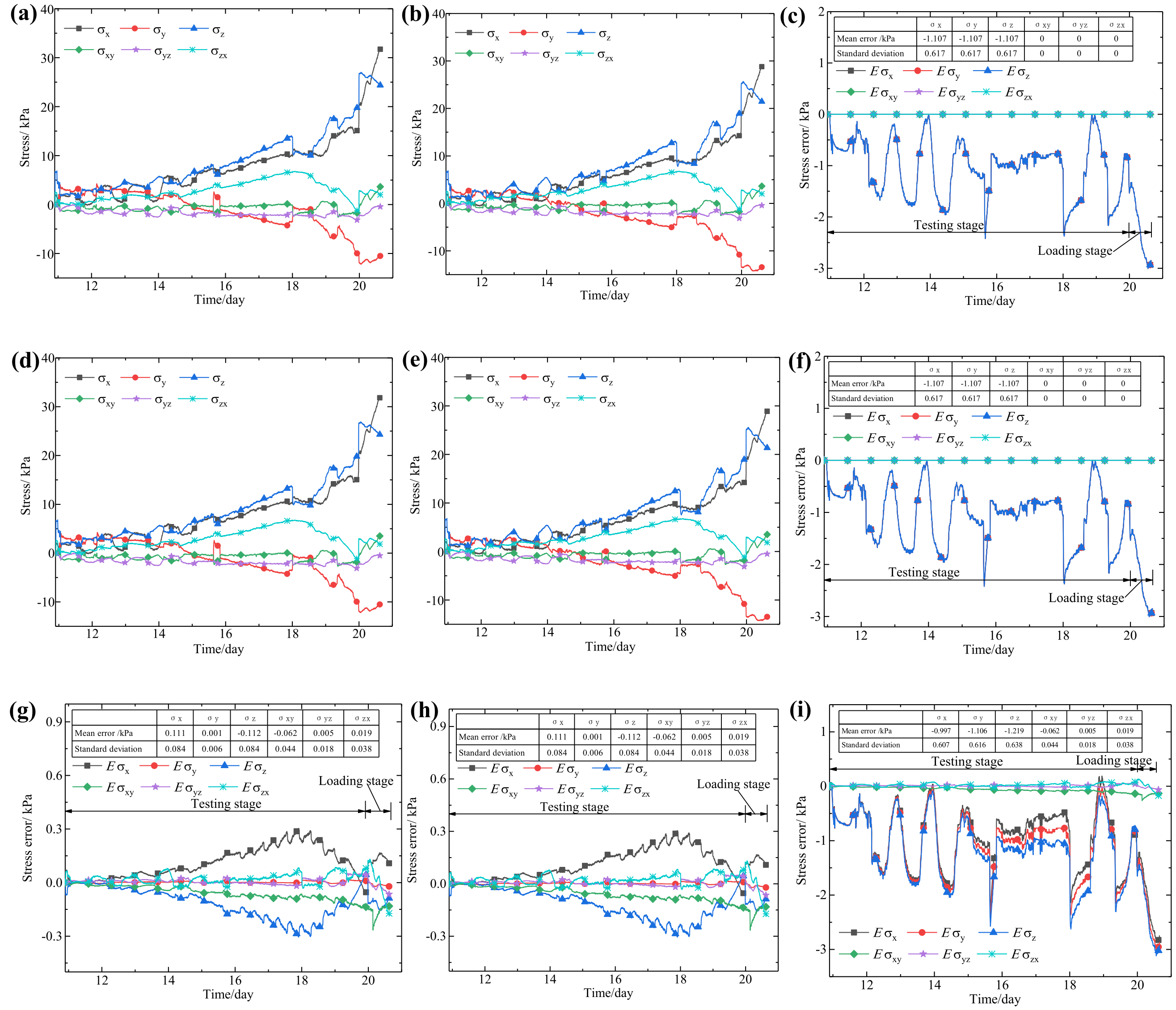

Fig. 11 Calculated results of the three-dimensional stress state of the up device: **a** total stress state [σ_{11}]; **b** effective stress state [σ_{12}]; c [σ_{12}]–[σ_{11}]; (d) total stress state considering rotation angles [σ_{21}]; (e) effective stress state considering rotation angles [σ_{22}]; (f) [σ_{22}]–[σ_{21}]; (g) [σ_{21}]–[σ_{11}]; (h) [σ_{22}]–[σ_{12}]; (i) [σ_{22}]–[σ_{11}]

K_0 tested by the oedometer and the φ tested by the triaxial test as their true values, respectively, the relative errors of K_0 and φ can be calculated (Table 3).

Figure 13 and Table 3 show that, the test values and calculate values of K_0 are between 0.414 and 0.498, and those of φ are between 30.1° and 35.9°. The determination coefficient ($R^2 = 0.204$) of the K_0 values calculated by σ_y/σ_Z is distorted, which cannot reflect the tailings behavior as a whole, while the K_0 value (0.423) obtained by some stages is equal to that (0.423) obtained by σ_x/σ_Z. The discharge process of tailings has little difference from the consolidation process of soils, i.e., the latter first has a soil loading process, while the former nearly has no initial load. When the upper load and the soil thickness is small, the relationship between σ_x and σ_Z has a poor correlation, thus, the liner relationship between σ_x and σ_Z are inconsistent in different stages, and the R^2 of σ_x/σ_Z in Fig. 13 has little value when setting inception as 0.

Table 3 shows that, for the K_0 values, a 2.17% relative error exists between the test result (0.414) of K_0 oedometer in the laboratory and the linear regression result (0.423) from the 3D earth pressure device in-situ test, and a 20.29% relative error exists between the K_0 oedometer value and the linear regression result (0.498) by setting inception as zero. For the friction angle, a 2.02% relative error exists between the test result (34.5°) of Triaxial test and the calculate value (35.2°) from K_0 tested by the 3D earth pressure device. In summary, most values of K_0 and

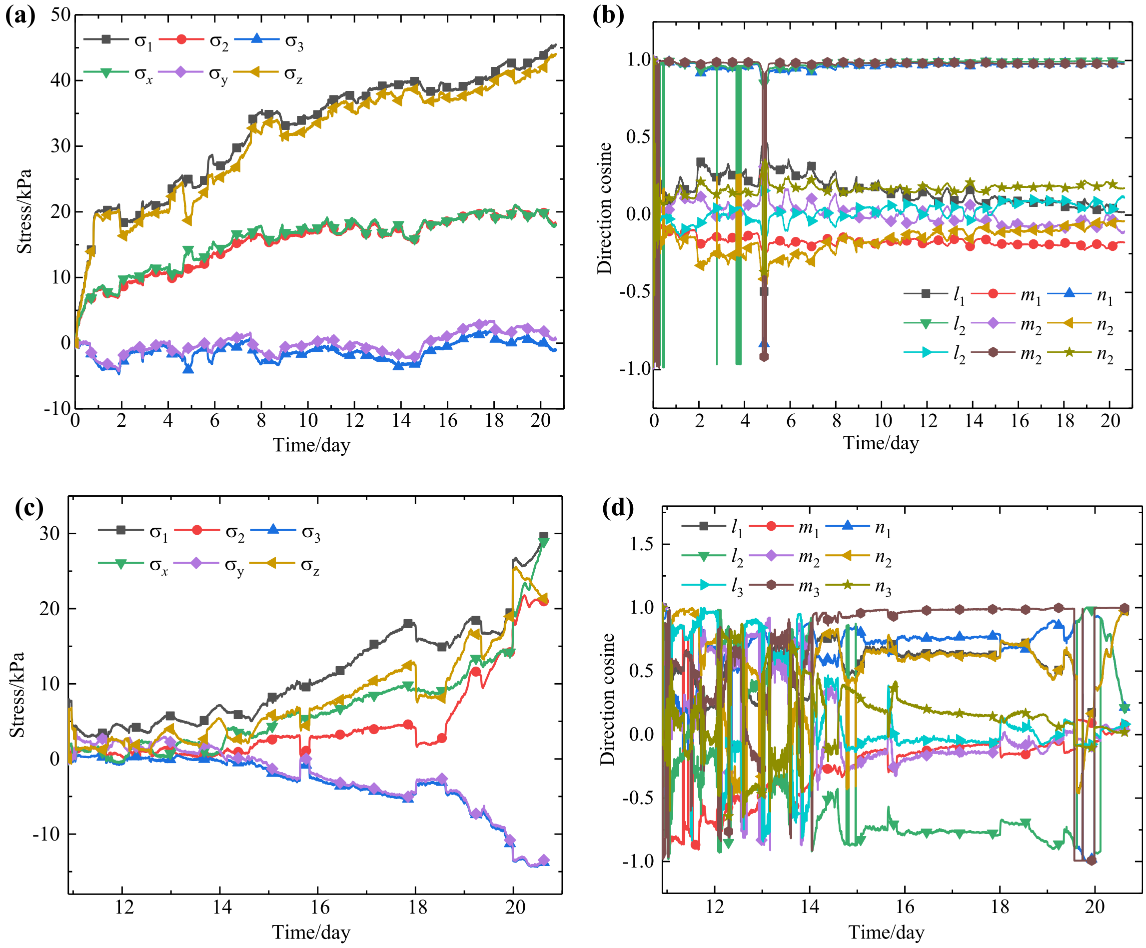

Fig. 12 Evolution law of principal stress and the stress direction: **a** principal stress of the bottom device; **b** directions of principal stress of the bottom device; **c** principal stress the top device; **d** directions of principal stress of the top device

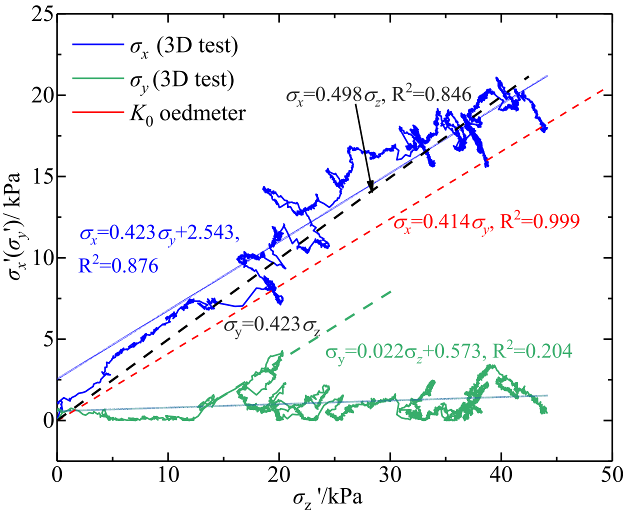

Fig. 13 Calculated and oedometer test value of K_0

φ determined by the 3D earth pressure device are mostly close to the values tested by the K_0 oedometer and triaxial test. Hence, the performance of the designed 3D stress state testing device is applicable in the model tests, and the three-dimensional stress state and the K_0 values can be determined by this method.

A few suggestions combined with the previous study [29] are summarized as follows: (1) The embedded depth should be greater than 2 times the size of 3D earth pressure device, i.e., 11 cm, to ensure that the stresses in all directions can be sensed at the same time. (2) The device can be directly used for testing after in-situ calibration and out of site calibration, and the angle is set to zero only as a selective operation. (3) Different upper loads should be provided to obtain the relationship between vertical force and lateral force, so the value of K_0 is calculated.

5 Conclusions

The relationship between the test direction and the three-dimensional stress state test is deduced. Considering the test errors caused by the rotation angles in the embedded and tested processes, the relationship between the absolute

Table 3 K_0 and the drained friction angle (φ)

Method	K_0			φ/°		
	Value	Relative error/%	Test/calculate method	Value/°	Relativeerror/%	Test/calculate method
σ_x/σ_Z	0.423	2.17	3D earth pressure device	35.2	2.02	Calculated by K_0
σ_x/σ_Z (setting inception as 0)	0.498	20.29	3D earth pressure device	30.1	12.76	Calculated by K_0
σ_y/σ_Z (stages values)	0.423	2.17	3D earth pressure device	35.2	2.02	Calculated by K_0
K_0 oedometer method	0.414	0.00	K_0 oedometer	35.9	3.86	Calculated by K_0
Direct shear test method	0.473	14.25	Calculated by φ	31.8	7.87	Direct shear test
Triaxial test method	0.433	4.59	Calculated by φ	34.5	0.00	Triaxial test

test direction and the relative test direction of the test device is derived to reduce the errors caused by the rotation angles.

A 3D earth pressure device is constructed by using a pedestal made by 3D printing technology, consisting of 6 earth pressure cells, a pore pressure cell and an attitude sensor, thus, the soil pressure in 6 directions, pore pressure, and the rotation angle of 3 axes can be tested with the 3D earth pressure device.

A method to reconstruct the space coordinate system is deduced based on the vector calculation and the method of Euler angle conversion, and the three-dimensional stress state in both the total stress form and effective stress form can be calculated dynamically.

A method to calculate the K_0 value is proposed based on the 3D earth pressure device. Comparing with the direct test result by the K_0 oedometer and indirect test results by direct shear test and triaxial test in laboratory, it indicates that the performance of the designed 3D stress state testing device is applicable.

The consolidation characteristics of tailings are significantly affected by external boundary conditions, the pore pressure has a significant effect on the three-dimensional stress state, and with the increase of pore pressure, the calculated errors of the three-dimensional stress state caused by rotation angles will be more noticeable.

Acknowledgements This work is supported by the National Key Laboratory Funding of Independent Research Project (No. S18406), National Natural Science Foundation of China (No. 41877251), National Natural Science Foundation of Liaoning (No. 2019-ZD-0187), and Tianjin Key Research and Development Project (No. 19YFZCSF00820). We would like to express our great acknowledgements to Benxi Iron & Steel Group who provided us many helps in the test process, and we wish to express our deepest gratitude goes to the anonymous reviewers and editors for their careful works and thoughtful suggestions that have helped improve this paper substantially.

References

1. Ahmed MR, Tran VDH, Meguid MA (2015) On the role of geogrid reinforcement in reducing earth pressure on buried pipes: experimental and numerical investigations. Soils Found 55:588–599
2. Ajovalasit A, D'Acquisto L, Fragapane S, Zuccarello B (2007) Stiffness and reinforcement effect of electrical resistance strain gauges. Strain 43:299–305
3. Borges JAR, Pires LF, Cassaro FAM, Roque WL, Heck RJ, Rosa JA, Wolf FG (2018) X-ray microtomography analysis of representative elementary volume (REV) of soil morphological and geometrical properties. Soil Tillage Res 182:112–122
4. Chernov IA (1991) Determination of transverse of resistor strain-gauges. Meas Tech USSR 34:249–253
5. Clayton CRI, Bica AVD (1993) The design of diaphragm-type boundary total stress cells. Geotechnique 43:523–535
6. Collins IF (1990) The nature of stress and velocity characteristics for critical stress states. Geotechnique 40:125–129
7. Fortuna S (2011) Validation of Lade's failure criteria at over-consolidated general stress states. J Geotech Geoenviron Eng 137:105–108
8. Fredlund DG, Rahardjo H (1993) Soil mechanics for unsaturated soils. John Wiley and Sons, New York
9. GBSL237-1999 (1999) Specification of soil test. China Water and Power Press, Beijing
10. Horn R, Johnson C, Semmel H, Schafer R, Lebert M (1992) Stress measurements in undisturbed unsaturated soils with a stress state transducer (SST): theory and 1st result. Zeitschrift Fuer Pflanzenernaehrung Und Bodenkunde 155:269–274
11. Hu N, Yu HS, Yang DS, Zhuang PZ (2019) Constitutive modelling of granular materials using a contact normal-based fabric tensor. Acta Geotech. https://doi.org/10.1007/s11440-019-00811-z
12. Huang S, Khan AS (1991) On the use of electrical - resistance metallic foil strain: gauges for measuring large dynamic plastic-deformation. Exp Mech 31:122–125
13. Jiang HW, Zhang JQ, Jiang RN (2017) Stress evaluation for rocks and structural concrete members through ultrasonic wave analysis: review. J Mater Civ Eng. https://doi.org/10.1061/(ASCE)MT.1943-5533.0001935
14. Jiang M, Zhu J, Chen S, Wang X, Guo W (2019) Experimental study on influence factors and empirical formula of K_0 for coarse grained soil. KSCE J Civil Eng 23:3305–3314
15. Kuhn MR, Sun WC, Wang Q (2015) Stress-induced anisotropy in granular materials: fabric, stiffness, and permeability. Acta Geotech 10:399–419. https://doi.org/10.1007/s11440-015-0397-5

16. Li JH, Zhang LM (2010) Geometric parameters and REV of a crack network in soil. Comput Geotech 37:466–475
17. Li X, Yu HS, Li XS (2009) Macro-micro relations in granular mechanics. Int J Solids Struct 46:4331–4341. https://doi.org/10.1016/j.ijsolstr.2009.08.018
18. Lim P, Tang L, Ni P (2019) Field evaluation of subgrade soils under dynamic loads using orthogonal earth pressure transducers. Soil Dyn Earthq Eng 121:12–24
19. Lu DC, Du XL, Zhou AN, Yao YP (2011) The principal stresses of soil mass in the direction of plane strain. Adv Mater Res 243–249:2657–2665
20. Mitchell JK, Kenichi S (2005) Fundamentals of soil behavior, 3rd edn. John Wiley and Sons Inc., Hoboken, New Jersey
21. Muszynski M, Olson S, Hashash Y, Phillips C (2016) Earth pressure measurements using tactile pressure sensors in a saturated sand during static and dynamic centrifuge testing. Geotech Test J 39:371–390
22. Palmer MC, O'Rourke TD, Olson NA, Abdoun T, Ha D, O'Rourke MJ (2009) Tactile pressure sensors for soil-structure interaction assessment. J Geotech Geoenviron Eng 135:1638–1645
23. Selig ET (1980) Soil stress gage calibration. Geotech Test J 3:153–158
24. Talesnick M (2005) Measuring soil contact pressure on a solid boundary and quantifying soil arching. Geotech Test J 28:171–179
25. Talesnick M, Horany H, Dancygier AN, Karinski YS (2008) Measuring soil pressure on a buried model structure for the validation of quantitative frameworks. J Geotech Geoenviron Eng 134:855–865
26. Talesnick M, Xia H, Moore I (2011) Earth pressure measurements on buried HDPE pipe. Geotechnique 61:721–732
27. Terzaghi K (1943) Theoretical soil mechanics. John Wiley and Sons Inc, New York
28. Weiler WA, Kulhawy FH (1982) Factors affecting stress cell measurements in soil. J Geotech Found Div ASCE 108:1529–1548
29. Wenxi Y (2019) Research on the application performance of three dimensional earth pressure device. Master dissertation, Tianjin Chengjian University
30. Zhao CG, Liu ZZ, Shi PX, Li J, Cai GQ, Wei CF (2016) Average soil skeleton stress for unsaturated soils and discussion on effective stress. Int J Geomech 16:D4015006
31. Zhu B, Jardine R, Foray P (2009) The use of miniature soil stress measuring cells in laboratory applications involving stress reversals. Soils Found 49:675–688

Publisher's Note Springer Nature remains neutral with regard to jurisdictional claims in published maps and institutional affiliations.